From Images to Azimuth: A Comprehensive Study of Orientation Calibration Techniques for the EXoplanet Climate Infrared TElescope (EXCITE)

by

Feifan Deng

A thesis submitted in partial fulfillment

of the requirements for the Degree of ScM

BROWN UNIVERSITY

May 2025

Acknowledgments

I would like to thank Professor Greg Tucker for providing me with the opportunity to work on this fascinating project and for his guidance throughout. I'm also grateful to the EXCITE team for creating such a supportive and collaborative environment. Special thanks to Tim for his crucial guidance at key moments, and to Annalies, Khing, Cait, and Oliver for being such kind and generous teammates—it was truly a joy to work with all of you.

Many thanks to my partner, Yiding Dai, for his constant encouragement and unwavering emotional support throughout this journey. His thoughtful help with physics concepts often brought clarity just when I needed it most. I'm lucky to have had him beside me every step of the way.

I would also like to thank my family and friends for their encouragement and understanding throughout this process. This thesis would not have been possible without their support.

Contents

List of Figures

Abstract of From Images to Azimuth: A Comprehensive Study of Orientation Calibration Techniques for the EXoplanet Climate Infrared TElescope (EXCITE), by Feifan Deng, Degree ScM, Brown University, May 2025

During the August 2024 test flight of the EXoplanet Climate Infrared TElescope (EXCITE), a balloon-borne observatory designed to characterize exoplanet atmospheres, absolute azimuth data from the on-board GPS compass was not available throughout the flight. To supplement the pointing information, we developed a method to reconstruct the payload's azimuth using images from a 360° action camera mounted externally on the gondola. The front-facing lens of the camera was approximately aligned with the forward (stern-bow) direction of the gondola.

Through a ground-based calibration test, we determined that the camera follows an equidistant projection model, allowing sun positions in the image to be mapped to azimuth angles with a resolution of 0.5°. An automated Python pipeline was created to detect and centroid the sun in each image and to assign an azimuth relative to the camera's reference frame. These relative angles were then combined with solar ephemeris data to recover the payload's absolute azimuth.

The image-derived azimuth was compared with the yaw data calculated from gyroscope integration. While the two datasets showed similar trends across the flight, a growing offset was observed in the later hours, likely due to integrated bias in the gyroscope solution. An additional elevation analysis using both encoder data and image-derived solar elevation helped confirm the accuracy of the elevation relative to the Sun. The secondary mirror temperature increase near 11:30 AM (GDT-6) is consistent with reconstructed pointing that placed the telescope closely aligned with the Sun within ±3° elevation and ±5° azimuth relative to the Sun.

This work demonstrates that 360° imaging, combined with basic calibration and supporting flight data, can provide a robust alternative means of azimuth reconstruction. The approach offers a valuable tool for future balloon missions where direct azimuth measurements may be limited or unavailable.

Chapter 1

Introduction

The **EXoplanet Climate Infrared TElescope (EXCITE)** is a balloon-borne experiment designed to study the atmospheres of exoplanets through high-precision spectroscopic measurements. The instrument consists of a semi-custom Ritchey-Chrétien telescope with a 0.5-meter primary mirror, housed within a gondola that also contains a cryogenic receiver and a high-precision pointing system. [1] During flight, the telescope continuously observes hot Jupiter exoplanets throughout their entire orbits, capturing spectroscopic phase curves that reveal the atmospheric composition and energy distribution of these distant worlds. [2]

In August 2024, the EXCITE team carried out a test flight from the NASA Columbia Scientific Balloon Facility (CSBF), stationed in Fort Sumner, New Mexico. The primary goal of the flight was to validate key systems under real flight conditions. However, one of the challenges encountered during the flight was the failure of the GPS compass system to provide absolute azimuth data. The telescope is equipped with three fiber optic rate gyroscopes that measure angular velocity and are typically used for feedback for the pointing system. They only provide relative changes in azimuth, not absolute direction. Since azimuth angles are essential for determining the telescope's orientation, this became a critical issue.

To address this issue, we investigated alternative methods to reconstruct the telescope's absolute azimuth throughout the flight. A 360° action camera (Insta360 One X) was mounted on the exterior of the gondola during the test, with its front lens roughly aligned with the gondola's stern-bow direction, estimated to within a few degrees. The stern-bow direction refers to the back-to-front axis of the gondola, which is shaped like a ship; this will be further explained and illustrated in Chapter 2.

In addition to the photos captured by this camera, we also retained estimated azimuth data measured by the gyroscopes, as well as GPS-based location data (latitude, longitude, and altitude). Two separate GPS units were provided by CSBF: the first was a Trimble differential GPS capable of delivering absolute azimuth measurements, but it ceased functioning immediately after launch. The second was a standard GPS unit that reliably provided location data throughout the flight, in this paper, we refer to it as the "location GPS."

The focus of my role in this project was to explore how these datasets, particularly the camera imagery, could be used to reconstruct the telescope's absolute azimuth angle during flight. The goal was to combine all available sources of information to estimate the payload's orientation as accurately as possible in the absence of a working compass. This thesis presents the methodology, implementation, and results of that effort.

Chapter 2

Instrumentation & Data Collection

The EXCITE payload is primarily made up of a gondola structure that supports all the major subsystems needed for the flight. These include the telescope, the pointing system, a cryogenic receiver, and various electronics for power, data handling, and communication. In particular, the pointing system consists of three gyroscopes, a boresight and a roll star camera mounted on the telescope baffle tube, as well as a tip/tilt system for fine guidance. Together, this integrated system is designed to enable long-duration observations of science targets, with pointing stability at the sub-arcsecond level.

The gondola is described using nautical terminology due to its elongated shape, which resembles that of a ship. As depicted in Figure 2.1, the bow refers to the front end of the gondola, while the stern refers to the back. The telescope is aligned along the stern-bow direction, as indicated by the arrow in Figure 2.1. The port side is the left when facing toward the bow, and the starboard side is the right. These terms provide a consistent way to describe the structure and orientation of the gondola.

To control and maintain the telescope's orientation during flight, the system rotates about three axes: yaw, pitch, and roll. These axes are illustrated in Figure 2.2. Yaw refers to the angle about the vertical axis of the gondola and is also known as the telescope's azimuth. Yaw control is achieved using a reaction wheel motor mounted at the bottom of the gondola and a pivot rotator

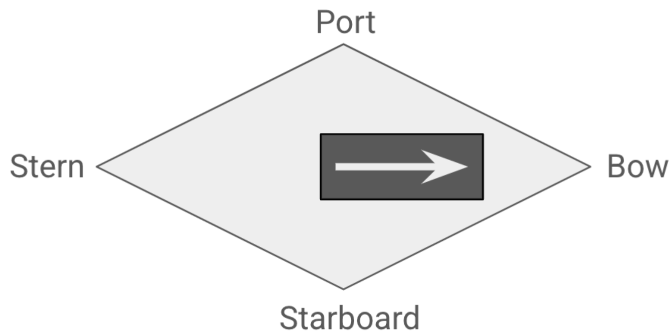

Figure 2.1: Simplified top-down illustration of the gondola (grey diamond). The stern, bow, port, and starboard directions are labeled. The black box represents the telescope, with the arrow indicating that the telescope boresight is in the stern-to-bow direction.

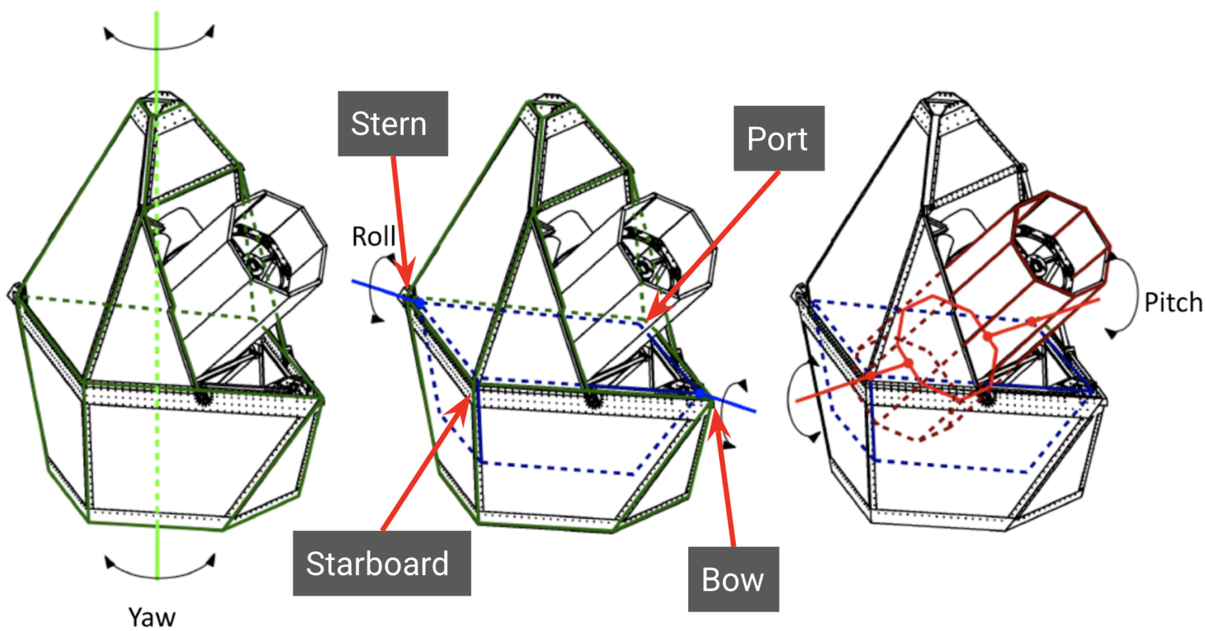

Figure 2.2: The telescope undergoes three rotational motions during flight: yaw (vertical axis, azimuth), roll (optical axis), and pitch (horizontal axis). Each axis is controlled independently to achieve precise pointing. [3]

which attaches to the balloon flight train. Roll is the angle about the stern-bow axis and pitch is the angle about the port-starboard axis, also known as the telescope's elevation. Both roll and pitch are driven by servo motors with limited range, each equipped with an encoder that records their angular position. All three axes can be commanded during flight to perform specific pointing maneuvers.

Unlike pitch and roll, yaw is not directly measured with an encoder. Instead, yaw motion is

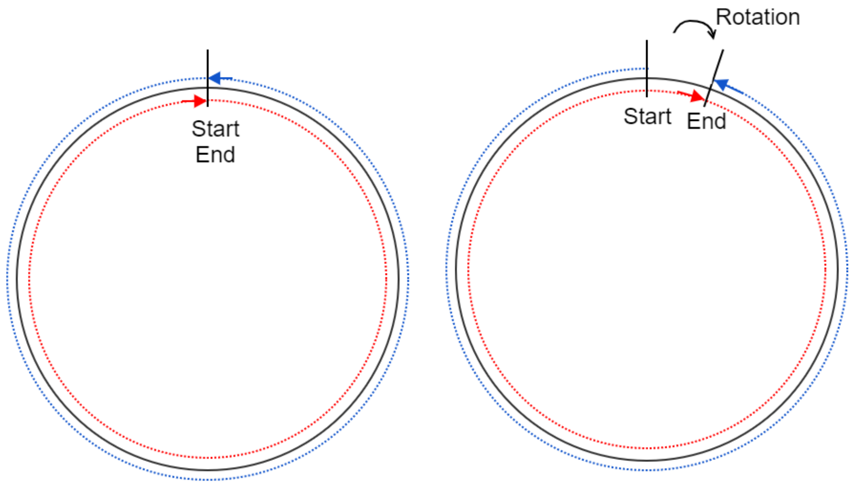

Figure 2.3: Illustration of the Sagnac effect: in the absence of rotation (left), light pulses traveling clockwise and counterclockwise return simultaneously. Under rotation (right), the path lengths differ, causing a measurable time shift that corresponds to angular velocity. [4]

calculated from the output of three orthogonally mounted fiber optic gyroscopes (iXblue iX-1B) using matrix-based processing. [5] In this paper, *yaw* refers specifically to the angle calculated from gyroscope data. The term *azimuth* is used exclusively for all other azimuthal measurements, including those obtained from the Trimble GPS and the 360° camera images.

Yaw data is not equivalent to the absolute azimuth of the payload. It is calculated by integrating rotational velocities measured by gyroscopes, which do not directly measure yaw and cannot provide an absolute yaw angle on their own. Instead, they track changes in orientation over time, and the resulting yaw value depends on an initial reference point. This reference value is changed each time the Master Control Computer (MCC) is powered on. To determine the absolute yaw at any given time, an external reference such as the azimuth derived from the camera at an earlier moment is required.

A gyroscope is a sensor that detects rotational velocity. These particular gyroscopes use the Sagnac effect, as illustrated in Figure 2.3. In this effect, light is split and sent through a coil in two opposite directions: one clockwise and the other counterclockwise. If the system is stationary, both light beams travel the same distance and arrive at the detector simultaneously. However, when the coil rotates, one path effectively becomes longer and the other shorter due to the motion. This creates a measurable time difference between the two light signals. The phase shift caused by the path length difference is proportional to the rate of rotation, allowing the system to accurately determine angular velocity.

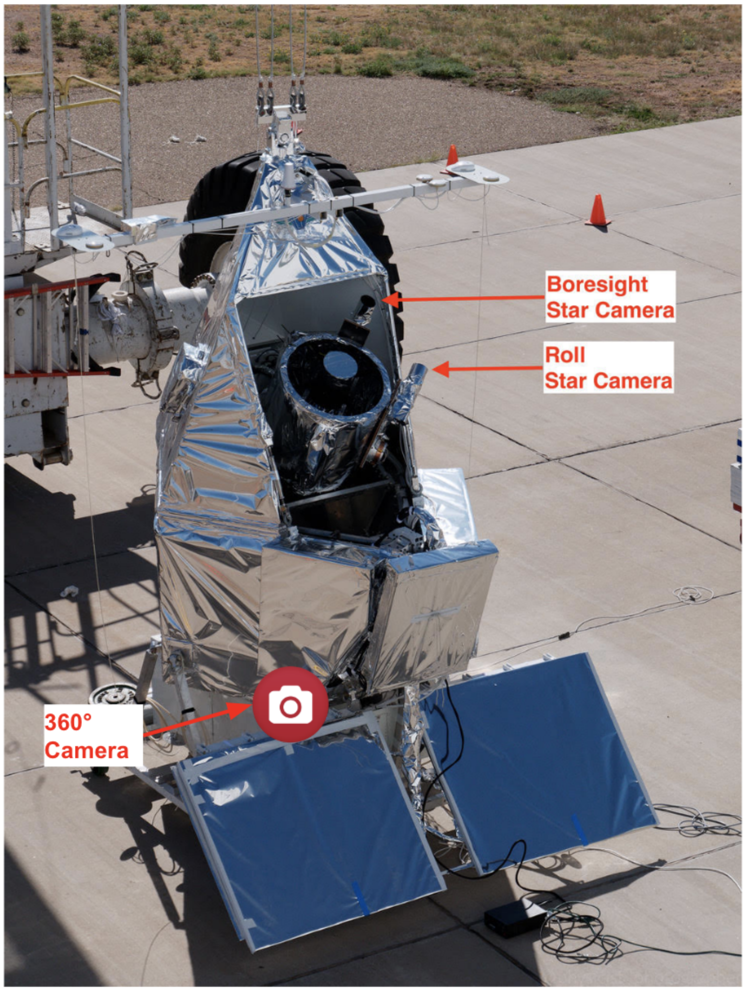

Figure 2.4: Star cameras are mounted on the telescope inside the gondola, with gyroscopes "Gyro-Y" and "Gyro-Z" positioned alongside each camera. The 360° camera is mounted externally on the front radiator panels of the gondola, providing a wide field of view.

Each gyroscope is mounted on a different part of the telescope: one is positioned at the back of the telescope, one on the boresight camera plate, and the last one is located on the roll camera plate. The locations of the two star cameras are shown in Figure 2.4. Although the gyroscopes are installed along orthogonal axes, none of them aligns perfectly with the yaw (azimuthal) direction. As a result, yaw estimation requires combining the outputs of all three gyroscopes while accounting for the telescope's current pitch and roll orientation. This coordinated processing is necessary because the gyroscopes measure angular velocity relative to the moving telescope frame, not the global reference frame.

The camera used for this study is a Insta360 One X, a 360° action camera equipped with two ultra-wide-angle lenses, each covering 200°. It was installed externally on the bow side of the gondola, mounted above the radiator panels, as shown in Figure 2.4. Limited by its placement, parts of the gondola structure are visible in the captured images. As a result, the gondola itself can obstruct the Sun at certain azimuth angles, blocking it from view. This effect will be further illustrated when analysing actual camera images in Chapter 3. In roughly half of the captured images, the Sun is either blocked by the gondola or obscured by clouds. It's important to note that cloud cover only occurred during ascent and descent, there were no clouds present while the payload was at float altitude (38 to 40 km).

Very little information is available regarding the Insta360 One X's lens type or projection model, also known as the mapping function. A mapping function describes how points in space (typically in angular coordinates like azimuth and elevation) are projected onto a flat image by a curved lens. For example, in a typical fisheye lens image, straight lines may appear curved, and equal angular separations in real space may not appear evenly spaced on the image. The type of mapping function used, such as equidistant, equisolid angle, stereographic, or rectilinear, has a significant impact on how accurately one can extract angular measurements from the image.

Since the mapping function is essential for determining the relative azimuth angle of the Sun, we conducted an experiment to classify it. We placed a series of evenly spaced visual markers along a flat wall at known azimuth angles, all at the same height as the camera to simulate objects at the horizon. The experimental setup is shown in Figure 2.5. After taking photos with the camera, we measured the pixel spacing between these markers in the resulting images. The consistent spacing indicated that the camera uses an equidistant projection, in which angular separations are preserved linearly in the image.

Based on this result, we constructed a projection grid by drawing a set of evenly spaced spherical wedges corresponding to constant azimuth angles, as shown in Figure 2.5. When a horizontal line

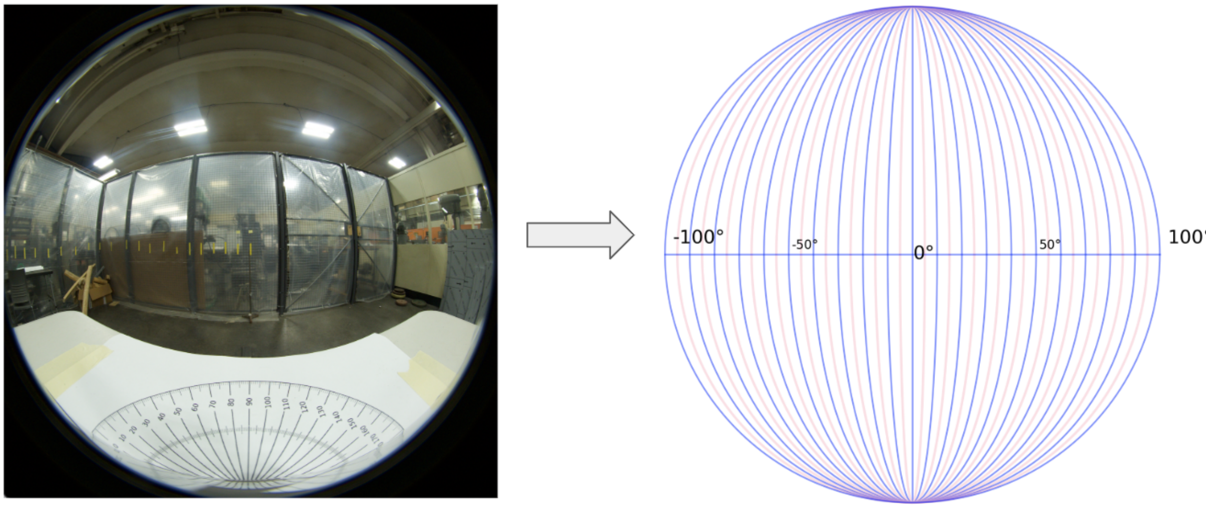

Figure 2.5: Left: image captured by the front-facing lens during the mapping function test. The camera is positioned at the center of a printed protractor, visible in the foreground for angular reference. Right: resulting azimuth grid map showing evenly spaced angles based on an equidistant projection.

(representing a rotation about the azimuth direction) is drawn across the wedges, its intersections with each wedge are evenly spaced, confirming the equidistant mapping. This grid was later used to calculate the relative azimuth of the Sun from image centroids during flight.

Chapter 3

Data Analysis Pipeline

To reconstruct the telescope's azimuth from the 360° camera images, we developed an automated image processing pipeline that detects the solar position in each frame and measures the corresponding angular displacement from the center of the camera. We custom wrote and debugged all functions used in this pipeline. The procedure was implemented in Python and followed these main steps:

1. **Sun Detection and Centroiding**

   The solar position was identified in each image using a two-stage detection algorithm. First, the detect_sun() function performed a coarse scan: it extracted the red channel from each image, leveraging the fact that the Sun typically saturates the red pixels. It scanned specified regions of the image (e.g., x = [1500:2600], y = [1:1350]) in steps of 20 pixels. When a saturated pixel (value equaling 255) was found, it verified that the surrounding area (approximately 40 pixels around the candidate point) was also saturated to confirm the detection. If the Sun was not detected in the first region, the algorithm continued searching in a second region.

   Once a potential sun pixel was identified, precise centroiding was performed using the find_sun_centroid() function: A square search area (typically 400 × 400 pixels) was defined around the detected candidate point. The cropped region was thresholded at a grayscale value of 200 to generate a binary image which isolates bright regions. Contours were extracted from the binary image, and the largest contour was assumed to represent the Sun. The centroid of this contour was computed using image moments, providing a sub-pixel-accurate (x, y) location of the Sun in the original image.

If no suitable contour was found, the algorithm returned a $None$ value for that image. This careful two-step process — coarse detection followed by fine centroiding — significantly improved robustness, particularly during changing lighting conditions throughout the flight.

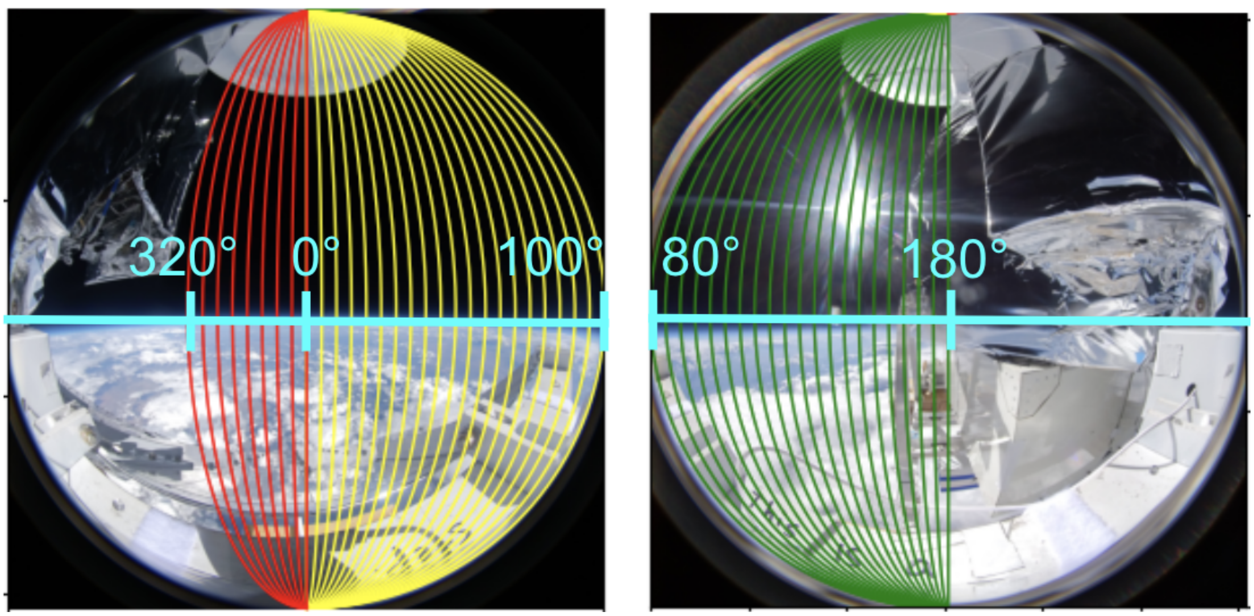

Figure 3.1: Illustration of azimuth angles measured by equidistant mapping on photos. Both photos were taken at the same time — the left by the front-facing lens and the right by the back-facing lens. The spherical wedges shown are drawn at 5° intervals in azimuth. At this timestamp, the Sun is detected at a relative azimuth of 147.5°

2. **Solar Azimuth Measurement**

After detecting the Sun's centroid, its angular position relative to the camera was calculated using the angle_measure() function. As mentioned in Chapter 2, the Insta360 One X has two lenses: one facing the front and the other facing the back. Thus, each image file produced by the camera contains two photos, one from each lens. We define the center of the front-facing lens as 0° in azimuth. To simplify the azimuth-finding pipeline, each image was divided into three regions based on the Sun's centroid (x, y) coordinates . As shown in Figure 3.1, these regions are outlined by spherical wedges of different colors, each corresponding to a specific range of azimuth values.

To determine the relative solar azimuth in the region where the Sun was detected, a set of spherical wedges was drawn by varying the minor axis length (e.g., from 0 to 1520 pixels) while keeping the major axis fixed at 1520 pixels. Along each wedge, the azimuth angle relative to the lens center was kept constant. The wedge with the closest distance to the Sun's centroid was selected, and the angle associated with that wedge was assigned as the solar azimuth relative to the camera for the image. The angle was measured at a resolution of 0.5°.

3. **Result Compilation & Data Export**

For each image, the filename, the image region where the Sun was detected (used for diagnostics), and the solar azimuth relative to the camera were recorded. If an image failed at either the detection or centroiding step, appropriate placeholder values were logged to preserve dataset consistency. After processing all images, the collected results served as the input for the subsequent azimuth reconstruction analysis. Robust error handling ensured that isolated failures did not interrupt the processing of the full image dataset.

Chapter 4

Results & Discussion

4.1 Gyroscope Yaw Data Analysis and Drift Correction

Before analyzing the azimuth angles measured from the 360° camera photos, we first examine the yaw rotation measured by the gyroscopes. This analysis provides a baseline for comparison with photo-derived azimuths and offers a potential fallback for periods during which the Sun is not visible in the camera images. A notable feature of the raw yaw data is a constant linear drift observed before launch. Although the telescope remained stationary in yaw during this time, the data shows an average decrease of 7.9° per hour. This drift indicates a systematic bias, which is consistent with the known design characteristic of the pointing system: the gyroscopes are biased whenever they are turned on. That bias can only be fully removed when the star cameras are locked onto a star.

To determine the telescope's absolute azimuth position during the pre-launch period, we refer to measurements from the Trimble GPS unit mounted on the payload. The Trimble GPS provided accurate azimuth data up until launch at 07:23 local time, after which it unexpectedly stopped recording. As shown in Figure 4.1, the azimuth reading remained relatively stable during the stationary pre-launch period, supporting the assumption that the telescope's yaw should not have changed. It is important to note, however, that the azimuth measured by the Trimble GPS does not

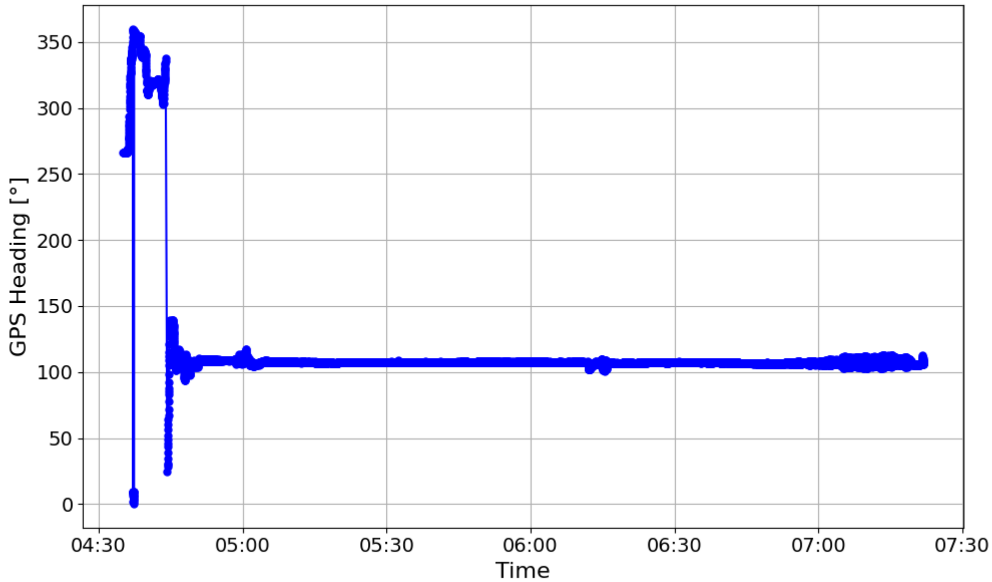

Figure 4.1: Trimble GPS azimuth from 04:30 – 07:30 local time. After the transport-related swings before 04:45, the azimuth remains stable near 110° until launch.

directly correspond to the true payload azimuth, as there is a default offset of -90° inherent in the system. The initial portion of the Trimble data, prior to 04:45 local time, captures the azimuthal changes of the payload as it was transported by vehicle to the launch site. Once in place, the payload's orientation remained fixed until launch.

To correct the yaw drift due to gyroscope bias, a linear fit was applied to the pre-launch yaw data, producing a detrended version shown in Figure 4.2. This process effectively flattens the yaw signal before launch. The time of launch is marked by the red dashed line. Post-correction, the pre-launch data reveals several stable periods, punctuated by abrupt changes. These discontinuities correspond to restarts of the MCC, which reset the yaw reference each time.

Unlike the pre-launch period, the yaw position during flight, spanning from 07:23 to approximately 17:00, remained continuous, as there is no record of the MCC restarting mid-flight. During ascent, the payload rotates uncontrolled until it reaches float altitudes. As seen from Figure 4.2, yaw exhibits full-range rotations between -180° to 180° from launch until about 11:00.

After 11:00, the yaw data show signs of stabilization beginning around 11:20. Notably, a gradual increasing trend is evident from 14:00 onward, and this trend will be confirmed by independent azimuth measurements obtained from image analysis in Section 4.2.

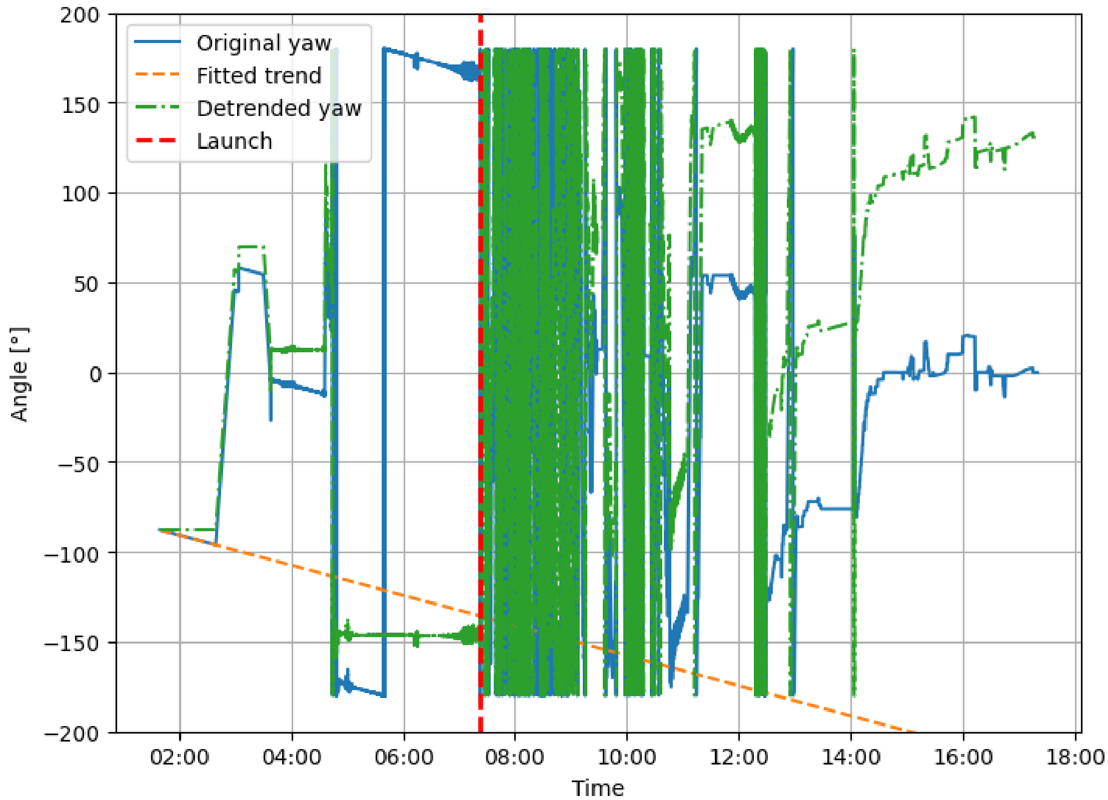

Figure 4.2: Original yaw data measured by the gyroscopes (blue), fitted linear drift (orange dashed), and detrended yaw (green) for the full observation period.

4.2 Image-Derived Payload Azimuth and Comparison with Yaw Data

Figure 4.3 shows the solar azimuth relative to the camera extracted directly from the flight images using the pipeline described in Chapter 3. Azimuth is defined clockwise from 0° to 360°, with 0° chosen at the center axis of the front-facing lens. Consequently, values near 0° or 360° indicate that the Sun appears close to the center of the front lens and, by extension, that the telescope is pointed almost directly toward the Sun. Conversely, values near 180° indicate that the telescope is pointed away from the Sun, which would be more suitable for observing exoplanet systems in future science

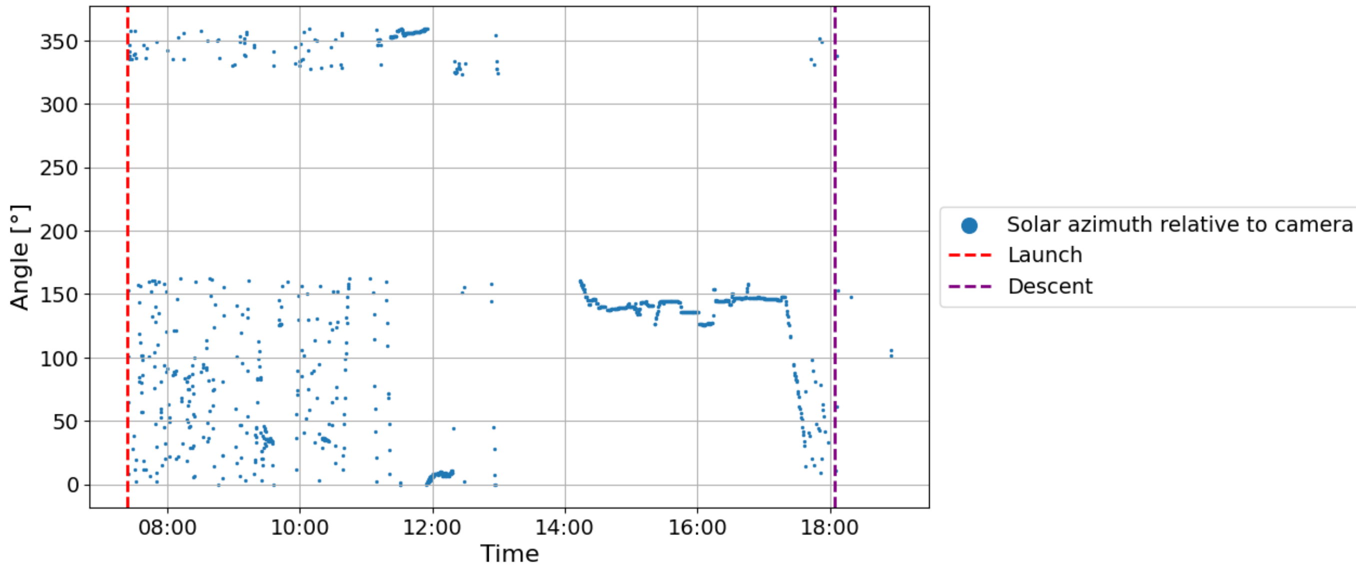

Figure 4.3: Measured solar azimuth relative to the camera's front-facing axis. Launch and descent times are marked with red and purple dashed lines, respectively.

missions. During the flight we processed 2000 photographs and recovered 1019 reliable azimuth measurements; the remainder lacked a usable solar centroid. The gap between 160° and 325° in Figure 4.3 corresponds to periods when the gondola obstructed the Sun.

Because the time stamps of the photographs depend on the camera's autonomous triggering, the sampling is irregular, ranging from 10 s to 30 s with an average of 21.8 s. Nevertheless, the data reveal several key azimuth states. Most importantly, after a series of deliberate "look-away" maneuvers, we achieved a stable anti-solar pointing of roughly 150° between 14:00 and 17:00, confirming that the maneuvers were successful.

To better understand the telescope's pointing throughout the flight, we calculated the absolute azimuth of the payload, θ_{Payload}. This was done by taking the difference between the solar azimuth relative to the camera, $\theta_{\text{P}\to\text{S}}$, which was measured from the photos, and the absolute solar azimuth in Earth's reference frame, θ_{Sun}.

$$\theta_{\text{Payload}} = \theta_{\text{Sun}} - \theta_{\text{P}\to\text{S}}$$

θ_{Sun} was calculated based on the time and geographic location of the payload throughout the flight using Astropy. θ_{Payload} is shown as the black scatter plot in Figure 4.4. The blue curve in the same plot shows θ_{Sun} over time.

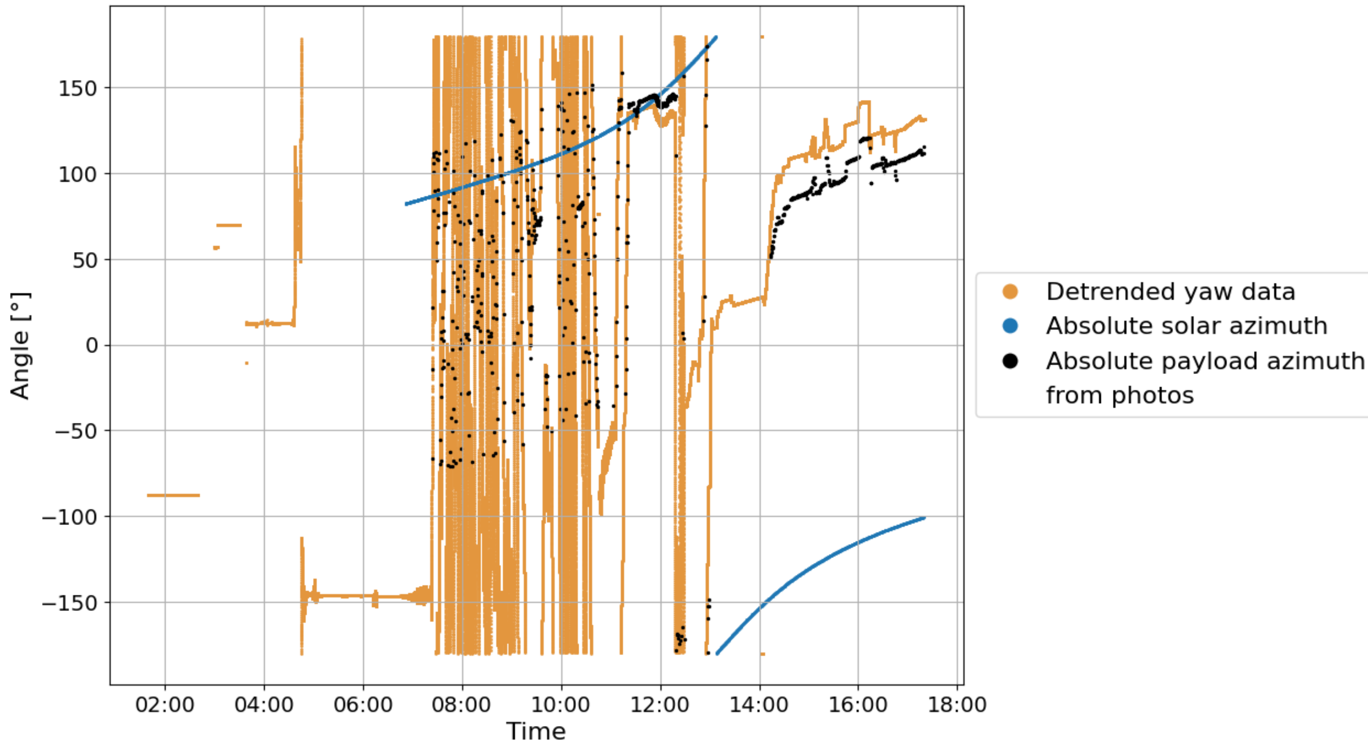

Figure 4.4: Comparison of detrended yaw data (orange), absolute solar azimuth θ_{Sun} (blue), and absolute payload azimuth θ_{Payload} derived from photos (black).

Since the camera is not perfectly aligned with the telescope's optical axis, a small correction was applied to account for this fixed offset (5.97 ± 2°). This offset was estimated by comparing known landmarks captured in the camera images at launch and was factored into the calculation of the payload's azimuth to better match the actual telescope orientation. When we compare the payload azimuth obtained from photos (black scatter plot) with the detrended yaw data (orange scatter plot), we find that the two agree fairly well in shape but differ in exact values. Notably, between approximately 11:30 and 12:00, the two datasets are in close agreement. However, starting around 14:00, a clear offset begins to appear between them, and this discrepancy remains constant toward the end of the flight.

There is some level of uncertainty in the azimuth measurements derived from the photos, but it is estimated to be no more than about 2°, which is much smaller than the gap observed (average of

20°) between the two datasets in the later part of the flight. This suggests that the mismatch likely does not originate from errors in the photo-based method.

It is worth noting that yaw data is not equivalent to the absolute azimuth of the payload. Yaw is calculated from the rotational velocities measured by the gyroscopes, and its zero point is redefined each time the MCC is powered on. In contrast, the azimuth values measured from the photos are more direct and rely less on cumulative calculations, making them less susceptible to long-term drift or integrated bias.

During standard flight operations, once the star cameras have locked on to stars, their pointing solution overrides the gyroscope yaw solution, which would eliminate the integrated bias error causing the offset in Figure 4.4. Unfortunately, the star cameras never solved during the test flight, so the gyroscope bias affected the yaw data for the entire flight. During flight, the gyroscope bias may have become nonlinear due to large slews that occurred between 12:00 and 13:00, so a linear subtraction might not have fully removed the bias. The gyroscopes are mounted on plates that hold the boresight and roll star cameras, and there could be slight misalignments in their mounting that could cause an offset in the resulting yaw calculation.

Further investigation, ideally through controlled ground-based experiments, could help identify the root cause of the discrepancy between the payload azimuth derived from images and that calculated from gyroscope data.

4.3 Elevation Analysis

To evaluate the telescope's elevation position, we also carried out a solar elevation analysis using a pipeline similar to that used for azimuth measurements from the photos. The goal was to extract the elevation angle of the Sun as seen by the 360° camera and compare it with the calculated absolute solar elevation based on time, latitude, longitude and altitude from the location GPS.

Figure 4.5 shows the results of this comparison. The blue curve represents the absolute solar elevation throughout the flight, computed using Astropy, by accounting for the payload's geographic

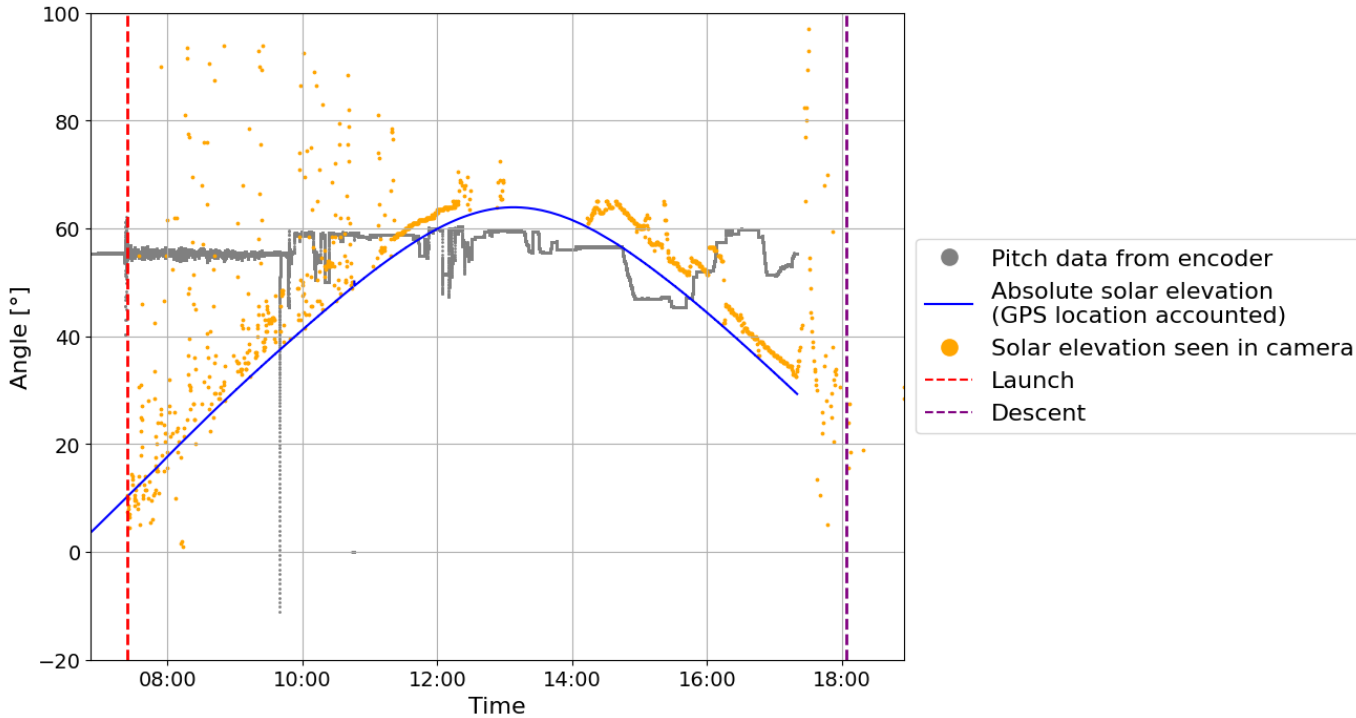

Figure 4.5: Comparison of absolute solar elevation (blue), solar elevation seen in the camera (orange), and telescope pitch data measured by the pitch encoder (grey).

location. The orange scatter points correspond to the elevation of the Sun measured directly from the images. In general, the camera-derived solar elevation follows the absolute elevation trend well.

The pitch of the telescope is shown in Figure 4.5 as the grey scatter plot. Here we use the term ”pitch” to exclusively refer to the data obtained directly from the telescope’s pitch encoder, to differentiate it from other elevation data. Only the telescope itself undergoes pitch changes, meaning that the Sun’s apparent elevation from the gondola’s perspective remains largely consistent with the true solar elevation.

However, some deviations are visible in the orange points, especially during the first half of the flight, where a number of data points stray as high as 90°. These outliers likely result from inaccurate measurements caused by lens flare or the Sun appearing near the edge of the frame, where distortions are more severe and centroiding is less reliable. It should also be noted that the camera may be not mounted fully flush with the gondola and it might be pointed slightly downwards. This may explain the camera-derived elevations being slightly overestimated.

While the current method provides a working estimate, the elevation detection algorithm can still be improved. For instance, in cases when the Sun is visible in both the front- and back-facing lenses—typically when it's near the edge of the camera's field of view—additional processing steps could help resolve its position more accurately. Furthermore, incorporating the effects of roll and yaw into the elevation estimation could refine the results, especially during dynamic maneuvers.

That said, this elevation analysis from photos serves mainly as a proof of concept. For practical purposes, the pitch data from the telescope's pitch encoder are more accurate and reliable. By combining the absolute solar elevation, the telescope pitch, and the azimuth information discussed earlier, we can determine how closely the telescope was pointed toward the Sun at different times during the flight—an important factor in evaluating the success of "look-away" or solar tracking maneuvers.

4.4 Thermal Effects of Telescope Orientation

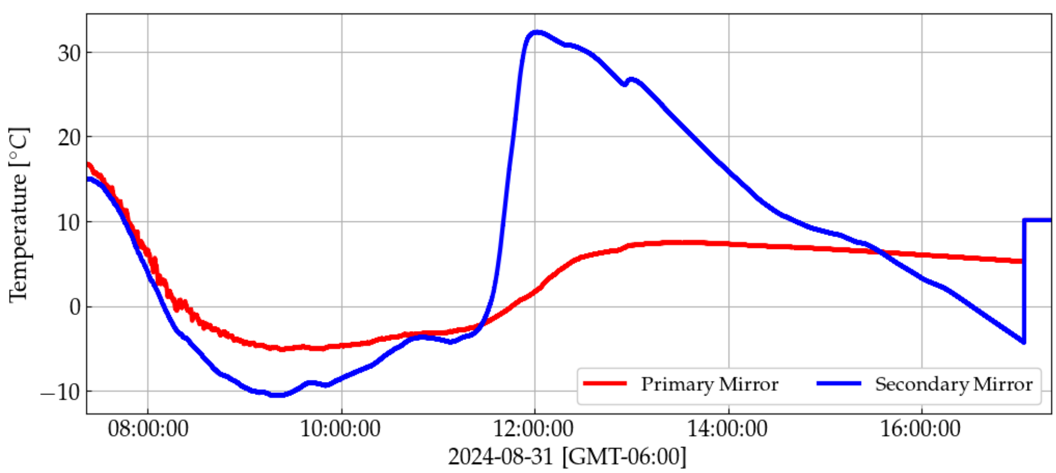

Figure 4.6: Temperature profiles of the primary (red) and secondary (blue) mirrors. A distinct increase is seen starting around 11:30 local time, which coincides with the telescope pointing directly at the Sun. [6]

A noticeable rise in the temperature of the secondary mirror was observed at around 11:30 local time, as shown in Figure 4.6. The temperature increase in the primary mirror is consistent with what would be expected from the ambient temperature rise during ascent into the stratosphere.

However, the secondary mirror exhibited a significantly larger increase. Since the secondary mirror extends beyond the telescope baffle, this raised the possibility that it may have been directly exposed to the Sun. To investigate this, we used orientation data from earlier analyses to determine whether the telescope was in fact aligned with the Sun at that time.

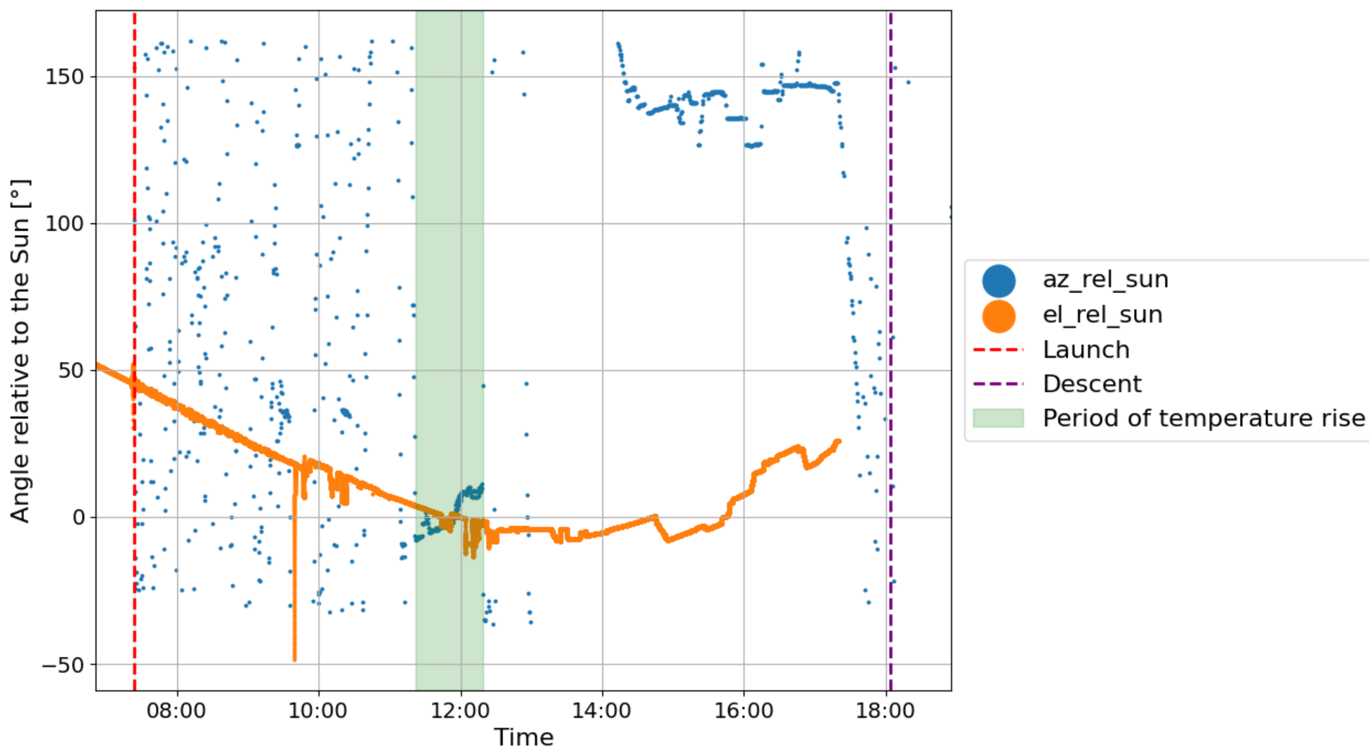

Figure 4.7: Azimuth (blue) and elevation (orange) of the telescope relative to the Sun during flight. The green shaded region highlights the time period of the secondary mirror temperature rise. During this time, both angles are near zero, confirming that the telescope was pointed nearly directly at the Sun. Launch and descent times are marked by the red and purple dashed lines, respectively.

To do this, we plotted the azimuth and elevation of the telescope relative to the Sun, denoted as *az_rel_sun* and *el_rel_sun*, respectively. *az_rel_sun* was taken from the photo-based azimuth measurements, while *el_rel_sun* was calculated as the difference between the telescope's pitch (from encoder data) and the absolute solar elevation.

The resulting plot, shown in Figure 4.7, confirms that both relative azimuth and elevation were near zero between approximately 11:30 and 12:00. This indicates that the telescope was indeed pointing very close to the Sun during that window, supporting the hypothesis that direct solar exposure contributed to the observed temperature increase. This result provides a strong validation of the orientation determination methods and analysis presented throughout this work.

Chapter 5

Conclusion

In this thesis, we developed and implemented a method to reconstruct EXCITE's azimuth during its August 2024 test flight, after the failure of the on-board Trimble GPS that provides azimuth measurements. Using a 360° camera mounted on the gondola, along with gyroscope data and location data from another on-board GPS, we successfully estimated the telescope's absolute azimuth over the course of the flight.

A key step was characterizing the camera's projection model. Through a controlled experiment, we found that it followed an equidistant projection, allowing us to map solar positions in images to azimuth and elevation angles with 0.5° resolution. A custom pipeline was built to detect and centroid the Sun in each frame and convert that to angular measurements. These were then aligned with Earth-based solar azimuths to produce absolute azimuth estimates.

Comparisons with gyroscope-derived yaw data showed broad agreement in shape but revealed increasing discrepancies later in the flight, likely due to accumulated integrated bias. We also validated our results with supporting elevation data and identified a period of direct solar pointing that corresponded to a sharp rise in the secondary mirror temperature.

In conclusion, this work demonstrated that a 360° camera can serve as an effective backup tool for reconstructing payload azimuth in high-altitude balloon experiments. By combining relatively simple instrumentation with careful calibration and image analysis, we were able to recover critical orientation data despite hardware failures. Future improvements could focus on refining sun detection under edge conditions, incorporating roll effects into elevation estimation, and validating the full system through ground-based experiments. These enhancements would further increase the reliability of orientation determination in balloon-borne missions like EXCITE.

Bibliography

[1] Rehm, T., Bernard, L., Bocchieri, A., Butler, N., Changeat, Q., D'Alessandro, A., Edwards, B., Gamaunt, J., Gong, Q., Hartley, J., Helson, K., Jensen, L., Kelly, D., Klangboonkrong, K., Kleyheeg, A., Lewis, N., Li, S., Line, M., Maher, S., Waldmann, I. The Design and Development Status of the Cryogenic Receiver for the EXoplanet Climate Infrared TElescope (EXCITE). *Proc. SPIE*, Vol. 12190, 121900A (2022). https://doi.org/10.1117/12.2629588

[2] Nagler, P. C., Bernard, L., Bocchieri, A., Butler, N., Changeat, Q., D'Alessandro, A., Edwards, B., Gamaunt, J., Gong, Q., Hartley, J., Helson, K., Jensen, L., Kelly, D. P., Klangboonkrong, K., Kleyheeg, A., Lewis, N. K., Li, S., Line, M., Maher, S. F., McClelland, R., *et al.* The EXoplanet Climate Infrared TElescope (EXCITE). *Proc. SPIE*, Vol. 12184, 121840V (2022). https://doi.org/10.1117/12.2629373

[3] Nagler, P. *The EXoplanet Climate Infrared TElescope (EXCITE) Experiment*. Presentation, NASA Goddard Space Flight Center, 31 January 2020. Available via internal collaboration materials.

[4] SBG Systems. *What is a Gyroscope? Understanding Gyroscopic Sensors*. Available at: Available at: https://support.sbg-systems.com/sc/kb/latest/inertial-measurements-units/gyroscopes

[5] Romualdez, L. J. *Design, Implementation, and Operational Methodologies for Sub-Arcsecond Attitude Determination, Control, and Stabilization of the Super-pressure Balloon-borne Imag-*

ing Telescope (SuperBIT). Ph.D. thesis, Department of Aerospace Science and Engineering, University of Toronto, 2018.

[6] Rehm, T. *The EXoplanet Climate Infrared TElescope (EXCITE).* Ph.D. thesis, Department of Physics, Brown University, 2025.